

Doping Topological Dirac Semimetal with magnetic impurities: electronic structure of Mn-doped Cd_3As_2

H. Ness,¹ I. Leahy,² A. Rice,² D. Pashov,¹ K. Alberi,² and M. van Schilfgaarde²

¹*Department of Physics, King's College London, Strand, London WC2R 2LS, UK*

²*National Renewable Energy Laboratory, Golden, Colorado 80401, USA*

The prospect of transforming a Dirac topological semimetal (TSM) into a Weyl TSM phase, following doping by magnetic impurities, is central to TSM applications. The magnetic field from polarized d levels of magnetic impurities produces a field with a sharp local structure. To what extent magnetic impurities act in the same manner as an applied field and what are the effects of such a field on the electronic structure of a Dirac TSM is the subject of this paper. We present electronic structure calculations of bulk Cd_3As_2 with substitutional doping of Mn impurities in the dilute alloy range. Quasi-particle GW (QSGW) *ab-initio* electronic structure calculations are used in conjunction with $k \cdot p$ model Hamiltonian calculations. As expected, we observe the splitting of the Dirac points into pairs of Weyl points following the doping with Mn. We also show that the electronic structure of Mn-doped Cd_3As_2 can be emulated by the electronic structure of pristine Cd_3As_2 with an appropriate external magnetic field. Some properties of the conductivity of bulk Cd_3As_2 for different magnetic field orientations are also investigated. Our results inform future opportunities for unique device functionality based on band structure tuning not found in conventional magnetic Weyl TSM.

Keywords: electronic structure, density functional theory, many-body perturbation theory, model Hamiltonians, quantum materials, topological semimetals

I. INTRODUCTION

Three dimensional topological semimetals (TSMs) encompass a broad class of materials that are generally characterized by the presence of linear band touching nodes near their Fermi levels¹. These nodes are stabilized by the presence of specific symmetries. The exact details of their electronic structures, however, differ based on the combination of symmetries that are present, leading to several TSM sub-classes^{1,2}. While the sub-classes typically exhibit many similar properties (i.e., high carrier mobility or broadband absorption), differences can also support diverse phenomena that may be exploited for various applications^{1,3-6}.

An important question to ask is whether a TSM can be transformed from one sub-class to another by manipulating a specific symmetry. Such a capability can be advantageous for applications where it is desirable to add one or more properties. A prime example is the formation of a Weyl TSM from a Dirac TSM. Dirac TSMs exhibit both time reversal symmetry (TRS) and spatial inversion symmetry (IS) that help to support the presence of fourfold degenerate bands at the Dirac node(s) located along some high symmetry line(s) in reciprocal k -space. When either TRS or IS is broken, the Dirac nodes are instead represented as constituent Weyl nodes (with twofold band degeneracy and opposite chirality). Weyl TSMs exhibit several properties that are not present in Dirac TSMs, including robust Fermi arc surface states, the chiral anomaly, the anomalous Hall effect and the bulk photovoltaic effect¹.

An example of such a Dirac to Weyl TSM transformation was demonstrated in Bi-Sb compounds by Au ion implantation leading to IS breaking⁷. Attempts to transform the Dirac TSM Cd_3As_2 into a Weyl TSM EuCd_2As_2 , with the substitution of a magnetic element for Cd, have been made^{8,9}. However recent studies have shown that EuCd_2As_2 is a magnetic, small gap, semiconductor rather than a Weyl TSM¹⁰⁻¹².

It is therefore interesting to know if and how a Dirac TSM

can be transformed into a Weyl TSM through the addition of magnetic impurities. In the dilute alloy limit, such impurities have the potential to introduce a large local magnetic field and break TRS without significantly altering other aspects of the material structure. In this work, we explore and clarify the full extent to which substitutional doping with magnetic impurities transforms Dirac nodes into Weyl nodes and the relationships between the orientation of the magnetic moment, the electronic structure, and other properties, such as conductivity. We use Mn impurities in bulk Cd_3As_2 as a prototypical three dimensional Dirac system¹³. Cd_3As_2 ¹⁴ contains two Dirac points on the ΓZ line in the Brillouin zone, protected by the C_4 symmetry about z . For an ideal, undoped lattice, the Fermi energy E_F passes through the Dirac points.

As Mn and Cd both have two valence electrons, Mn substituting for Cd does not electrically dope Cd_3As_2 . However, Mn has a filled shell of 3d states in the majority channel, with the minority channel empty. Thus each Mn has a local magnetization of $5 \mu_B$, similar to MnTe. The majority and minority levels are split by a few eV roughly evenly about the Fermi energy according to the QSGW approximation described below. Thus both states are well removed from E_F and have little effect on states around E_F , except for the large effective magnetic field from the magnetization of the Mn d levels. The Mn local moment polarizes the Mn and As sp levels, and we may therefore expect it to behave similarly to an external magnetic field, breaking the TRS. To what extent Mn acts in the same manner as an applied field is a primary subject of this paper.

As we show below, the effective field generated by local moment can be very large compared to external fields accessible in the laboratory. However the net contribution from Mn will depend on the doping, and to what extent the Mn spins are ordered. For the low doping regime we consider here the spins should be completely disordered; however, the spin susceptibility will be greatly enhanced by the partial alignment of the spins on application of a field. For the electronic structure

we consider an idealized case: substituting a single Mn on a Cd site in the unit cell of Cd_3As_2 (i.e. doping $\sim 2\%$), aligned ferromagnetically.

We use *ab-initio* electronic structure calculations combined with model Hamiltonian calculations to understand the transformation of Dirac points into Weyl points in bulk Cd_3As_2 . We show that the electronic structure of Mn-doped Cd_3As_2 can be well reproduced from the electronic structure of pristine Cd_3As_2 with an appropriate external magnetic field. We also briefly study some properties of the conductivity of bulk Cd_3As_2 for different orientations of an applied magnetic field.

The paper is organised as follows: In Section II we present and discuss the results of our calculations for the electronic structure and the conductivity. Conclusions are presented in Section III. Additional information are provided in the appendices, about: technicality for the *ab-initio* calculations in Appendix A, the model Hamiltonian in Appendix B and linear response conductivity in Appendix C.

II. CALCULATIONS AND DISCUSSION

In this section, we show how the electronic structure of pristine Cd_3As_2 is modified by the inclusion of Mn magnetic impurities, i.e. the splitting of the Dirac points into pairs of Weyl points. We also study how an applied magnetic field can have similar effects on the band structures. The calculations are performed by using both an *ab-initio* electronic structure method and model Hamiltonians.

A. *Ab-initio* electronic structure

First principles electronic structure calculations have been performed using the Questaal package¹⁵. Questaal is an all-electron method, with an augmented wave basis consisting of partial waves inside augmentation spheres based on the linear muffin-tin orbital technique¹⁶. Calculations have been done at different levels of density functional theory (DFT), i.e. LDA and GGA. Going beyond DFT, we have also performed Quasi-particle Self-consistent GW (QSGW) calculations¹⁷. QSGW provides an effective way to implement the GW approximation without relying on a lower level theory as a starting point^{18,19}.

We consider a primitive unit cell, for bulk Cd_3As_2 , consisting of 80 atoms (48 atoms of Cd and 32 of As) as shown in panel (a) of Figure 1. See Appendix A for information about the unit cell and k -space mesh.

Before exploring the effects of Mn doping, we verify the known Cd_3As_2 band structure using both DFT and QSGW. Our DFT calculations (not shown) agree with previously reported band-structures^{20–26}. Figure 1 shows our QSGW calculated band structures. Panels (b) and (c) in Fig. 1 show the QSGW bands for undoped Cd_3As_2 . Two Dirac points (i.e. crossing of 4 degenerate bands of mostly 4p As character) are found at E_F along the Z Γ line, they are located at $k = (0, 0, \pm k_D)$ with $k_D \sim 0.029 \text{ \AA}^{-1}$, a slightly smaller value than those based on DFT calculations^{20–22,24}.

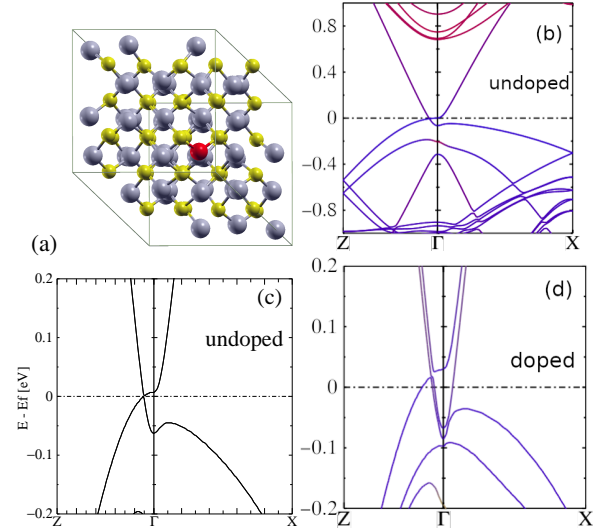


Figure 1. Panel (a): Ball-and-stick representation of the supercell for Cd_3As_2 . Cd atoms are shown in grey, As atoms in yellow. The red atom is Cd for the pristine structure, and is Mn for the 2 % doped crystal. Panel (b): QSGW electronic band structure of Cd_3As_2 for high symmetry k -space path ZTX. Energies, in eV, are measured from the Fermi level $E_F = 0$ reference energy where the Dirac point lies. The two Dirac points for the entire pristine Cd_3As_2 are located in k -space at $(0, 0, \pm k_D)$ with $k_D \sim 0.03 \text{ \AA}^{-1}$. Color weighting: red for Cd 5s orbital and blue for As 4p. Panel (c): Zoom in energy around the Dirac point. Panel (d): QSGW band structure of Mn-doped Cd_3As_2 around the Dirac point observed in the undoped case. Bands are split by a Zeeman-like effect due to the magnetic Mn impurity and the Dirac point seems to have disappeared.

The band velocity around the Γ -point and around the Dirac points are given in Table I for pristine Cd_3As_2 . The QSGW calculations provide, for at least one branch of the Dirac crossing bands, a velocity of $\sim 9 - 10 \times 10^5 \text{ [m/s]}$, in agreement with values found in the literature^{3,27,28}. By contrast, the band velocity is severely underestimated in DFT. This is to be expected because of the local potential DFT generates. DFT underestimates bandgaps in semiconductors²⁹ and the Fermi velocity at the Dirac point in graphene³⁰. A local LDA potential in the auxiliary DFT Hamiltonian results in underestimates of the bandgap, as clearly shown for a few semiconductors in Ref³¹.

Shortcomings in the LDA and GGA are also reflected in the location of the Cd 5s states: in QSGW they are higher in energy than in DFT. When these states are too low, they may repel the As 4p states and contribute to the underestimate of the Fermi velocity. Also admix too much of Cd s into the states in the vicinity of the Dirac point. Furthermore, the band inversion mechanism leading to the crossing at $k_z = k_D$ along the $(0, 0, \pm k_z)$ lines involves a parabolic and an inverted parabolic bands with mostly As 4p character. The effective mass of electron-like band is smaller than the effective mass of hole-like band, therefore around the Dirac point, one branch (annoted Z Γ down in Table I) of the crossing bands is associated with a larger velocity than the other branch (annoted Z Γ up in Table I).

We now turn to the case of Cd_3As_2 doped by magnetic impurities. We consider that, for the Mn-doped system, one Cd atom in the unit cell is replaced by Mn, i.e. corresponding to a doping of $1/48 \sim 2\%$. The band structure of the Mn-doped Cd_3As_2 is substantially different from the undoped system, see panel (d) in Figure 1. Bands are split by a Zeeman-like effect owing to the polarization of the As $4p$ states induced by the magnetic Mn impurity.

The Dirac point disappears from the symmetry protected $\text{Z}\Gamma$ k -space line. Gapped bands occur around $E - E_F = 25$ meV close to the Γ point on the $\text{Z}\Gamma$ k -path.

The majority(minority) Mn d states consists of occupied (empty) states, centered at $E_F - 4.5$ eV ($E_F + 3.5$ eV) respectively. They make the system ferromagnetic with a net moment of $5.0 \mu_B$. The Mn local moment in the Mn augmentation sphere is found to be $4.4 \mu_B$, the remaining $0.6 \mu_B$ decaying away from the Mn. According to the Stoner picture, we should expect the $d^\uparrow - d^\downarrow$ energy splitting to be $I \cdot M$, where I is the Stoner parameter and M the local moment. As a rule of thumb, $I = 1$ eV for $3d$ transition metals and would lead to $d^\uparrow - d^\downarrow = 8.8$ eV. Thus the Stoner splitting is qualitatively correct, though it overestimates slightly the actual splitting. Both d^\uparrow and d^\downarrow are very localized, each with a bandwidth of ~ 2 eV. The dispersion establishes that the Mn d band hybridizes to some extent with the Cd and As (the Mn-Mn separation is 12.6 \AA , too large for direct coupling) and induces a small local moment on those sites. Two of the four As nearest neighbors to Mn acquire a moment of about $0.025 \mu_B$. For comparison, the Mn local moment in LDA is calculated to be $3.9 \mu_B$ and the d^\uparrow and d^\downarrow band centers fall at approximately $E_F - 3.0$ eV and ($E_F + 1.0$ eV), respectively. The splitting is small enough that states near E_F have non-negligible Mn d character. This shows only that the LDA does not provide an adequate description of the magnetic electronic structure.

As previously mentioned, the magnetic field coming from polarized Mn d levels has a sharp local (in space) structure, somewhat different from what is expected from a macroscopic applied field. However, it is interesting to see to which extent this field acts in a similar manner as an applied external field.

In order to get more insight into the band structure of Mn-doped Cd_3As_2 , we consider next how the band structure of pristine Cd_3As_2 is modified by the presence of an applied external magnetic field (the latter emulating the presence of the Mn magnetic impurity).

Figure 2 shows the QSGW band structure of pristine Cd_3As_2 obtained in the presence of an external applied magnetic field B_{ext} oriented in the z -direction. Upon application of the magnetic fields, bands are split due to the Zeeman effect, as expected. A large external field, as large as 6 mRy (72.2 meV or 1249.1 Tesla), generated a Zeeman band splitting similar to what is obtained for the Mn-doped Cd_3As_2 system. For that field value, the band structure of pristine Cd_3As_2 bears some strong resemblance with the bands of the Mn-doped crystal; although missing the apparent gapped band around $E - E_F = 25$ meV seen in the Mn-doped case (comparing Figures 1(d) and 2(c)).

Energy range	k - path	QSGW	LDA	GGA
200 to 600 meV	$\text{Z}\Gamma$	9.2 – 10.6	~ 4.0	
	ΓX	7.5 – 9.1	~ 2.0	
10 to 25 meV	$\text{Z}\Gamma$ down	~ 9.0		~ 5.9
	$\text{Z}\Gamma$ up	~ 1.5		~ 1.5
Dirac point $k_D [\text{\AA}^{-1}]$		0.029		0.042

Table I. Band velocities (in units of 10^5 [m/s]) from QSGW and DFT band structure calculations of pristine Cd_3As_2 , for different k -paths and different energy ranges. And value of the Dirac point position $(0, 0, k_D)$ along ΓZ .

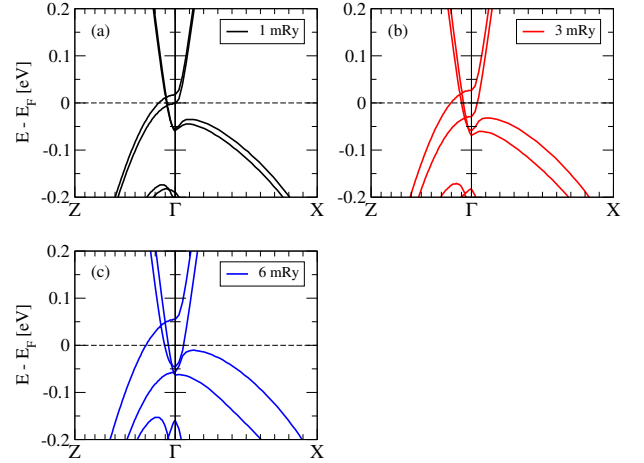


Figure 2. QSGW electronic band structure of pristine Cd_3As_2 in the presence of an external applied magnetic field B_{ext} , oriented in the z -direction. Energies, in eV, are measured from the Fermi level $E_F = 0$ reference energy. (a) $B_{\text{ext}} = 1$ mRy (13.6 meV or 235.8 Tesla), (b) $B_{\text{ext}} = 3$ mRy (40.8 meV or 705.8 Tesla), (c) $B_{\text{ext}} = 6$ mRy (72.2 meV or 1249.1 Tesla) which bears strong resemblance with the bands of Mn-doped Cd_3As_2 .

B. Model Hamiltonian: electronic structure and external magnetic field effects

From *ab-initio* calculations, we have seen that an applied field to the undoped Cd_3As_2 can generate similar bands to the Mn-doped Cd_3As_2 system. The next question to solve is what happens to the Dirac points in the presence of Mn-doping and/or of the applied magnetic field?

To answer this question, we turn to a simpler model to describe the band structure of Cd_3As_2 . Using such a model allows us to explore the k -space bands more easily and to consider any arbitrary magnitude and orientation of the magnetic field. We consider a $k \cdot p$ model consisting of four orbitals ($s, p_{x,y,z}$) and two spins for each orbital, and including a spin-orbit coupling term H_{SO} as described in Ref²⁰. Furthermore, we add a Zeeman-like term $H_B = -\gamma \mathbf{B} \cdot \boldsymbol{\sigma}$ where the magnetic field $\mathbf{B} = (B_x, B_y, B_z)$ couples to the spin Pauli matrices $\boldsymbol{\sigma} = (\sigma_x, \sigma_y, \sigma_z)$. The Hamiltonian $H_8(\mathbf{k})$ (of size 8×8) is a function of three components k_x, k_y, k_z of the crystal momen-

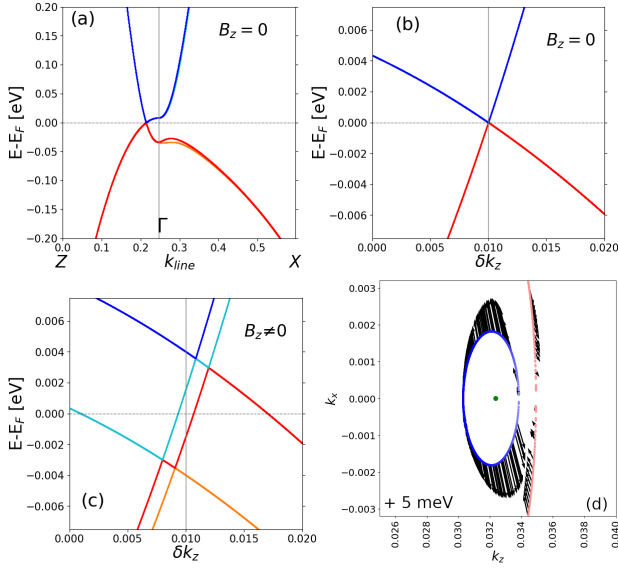


Figure 3. Band structure from Hamiltonian $H_8(\mathbf{k})$. (a) No applied field. Bands are colored according to the eigenvalues sorted in ascending order. The k -path k_{line} (in \AA^{-1}) goes from Z (left) to Γ (vertical black line), to X (right) as in Fig. 1. The Dirac point is along the ΓZ line, located at $k_D \sim 0.032 \text{ \AA}^{-1}$ away from Γ . (b) Zoom around the Dirac point along k_z (in \AA^{-1}) with $k_z = k_D - 0.01 + \delta k_z$. (c) Splitting of the Dirac point with an applied field $\gamma B_z = 4 \text{ meV}$ in the z -direction. The original Dirac point is split into a pair of Weyl points displaced away from $(0, 0, k_D)$ and slightly shifted in energy around E_F . (d) Two-dimensional constant-energy band structure in the $k_z - k_x$ plane around the Dirac point (green dot), for a constant energy $E - E_F = 5 \text{ meV}$. The band coloring corresponds to the value of the spin component S_z , i.e. blue $S_z = -1$, red $S_z = +1$, white $S_z = 0$. The black arrows are the spin vectors (S_y, S_x) in the $k_z - k_x$ plane.

tum \mathbf{k} , and is fully described in Appendix B. After diagonalization for each \mathbf{k} , the eigenvalues are used to build the corresponding band structure and additional physical quantities as detailed below. Such a model provides us with a quicker way to analyze how the Dirac points are displaced and/or split in k -space due to the application of the magnetic field.

Figure 3 shows the band structure obtained from the $k \cdot p$ H_8 Hamiltonian. In the absence of a magnetic field, the model provides a fairly good representation of the QSGW bands as can be seen by comparing Fig. 3(a) with the QSGW bands Fig. 1(c). With the $k \cdot p$ model, we obtain a Dirac point at $k_D = 0.032 \text{ \AA}^{-1}$, very close to the QSGW calculations.

Upon application of a magnetic field in the z -direction, the Dirac point is split into individual Weyl points³² displaced away from $(0, 0, k_D)$ and shifted symmetrically up and down in energy around E_F as shown in Figure 3(c). There are actually four band crossings, two above E_F and two below. Two corresponding to a pair of “conventional” Weyl points (Chern number ± 1) labelled W^\pm in Fig. 9, and two labelled C^\pm . Ref³² concluded that the C^\pm crossing points are “Weyl” points with Chern number 2. Our calculations align with Ref³² regarding the W^\pm points, but we do not find pronounced Berry curvature around the C^\pm points. This is discussed further in Appendix D.

The identification of the Weyl bands and crossings can be made clearly by considering the bands spin texture. The spin components S_i ($i = x, y, z$) are calculated from the expectation value of the spin Pauli matrices $S_i = \langle \sigma_i \rangle$ using the eigenstates of $H_8(\mathbf{k})$ at each \mathbf{k} point. In Appendix D, we provide a full analysis of the spin texture of the different bands and for different constant energies ranging from $E - E_F = 5 \text{ meV}$ to $E - E_F = -5 \text{ meV}$. Our analysis clearly identify the position of the Weyl points with opposite chirality. Figure 3(d) shows the two-dimensional constant-energy band structure, in the $k_z - k_x$ plane for a constant energy $E - E_F = 5 \text{ meV}$. The blue ellipse corresponds to a slice in the Weyl “cone” at $E - E_F > 0$, located around the original Dirac point (green dot in Fig. 3(d)). As discussed in the previous section, the bands around the Dirac points are anisotropic, i.e. they disperse with different velocities for different k orientation. Hence a constant energy slice in the Weyl “cone” has the shape of an ellipse, instead of a circle (were the velocity of the Weyl cone to be isotropic).

For $E - E_F = 5 \text{ meV}$, the constant energy ellipse has the spin component S_z oriented in one direction (opposite to the applied magnetic field) and anisotropic spin vectors (S_y, S_x) oriented outwards the ellipse in the $k_z - k_x$ plane. The outer (red) band ($k_z > 0.034 \text{ \AA}^{-1}$) shows a spin component S_z with the opposite direction and a different kind of spin texture. As detailed in Appendix D, the outer band corresponds to the second Weyl “cone” located below E_F around the original Dirac point.

Realistic band structure for real materials contains richer information in contrast to simpler band models considering only linear k -dispersion for the Weyl cones. The former may lead to transport properties which differ from those calculated from simpler bands (considering the change of velocity, spin texture with respect to change of Fermi energy or temperature).

So far we have considered the case of a magnetic field applied in the z -direction. It is crucial to know how the Dirac points are affected by a changing orientation of the field. Figure 4 compares how the Weyl points evolve from the Dirac points for fields along the x - and z -direction. For $\mathbf{B} \parallel z$, bands drawn along the $(0, 0, k_z)$ line, show that the Weyl points split in both k and energy, as shown in Figure 3. The separation between Weyl points is parallel to \mathbf{B} . When $\mathbf{B} \parallel x$, a gap appears on this same line; however, the Dirac point splits into two Weyl points at $(\pm \delta k_x, 0, \pm k_D)$. Fig. 4(c) depicts bands for the same excursion in k_z but offset by a fixed δk_x . In general the connecting vector between Weyl points is parallel to \mathbf{B} . However, the perturbation under a B_x field causes no energy splitting of the Weyl points, unlike the $\mathbf{B} \parallel z$ case.

Figure 5 shows constant-energy band in the two-dimensional $k_z - k_x$ plane around the pair of Weyl points located at $(\pm \delta k_x, 0, -k_D)$, moved along the x -direction of the field, in k -space. The spin texture is also represented for the three spin components $S_{x,y,z}$. The opposite chirality between the two Weyl points is clearly seen, as well as the change of sign of the spin texture for energy above and below the Weyl crossing points.

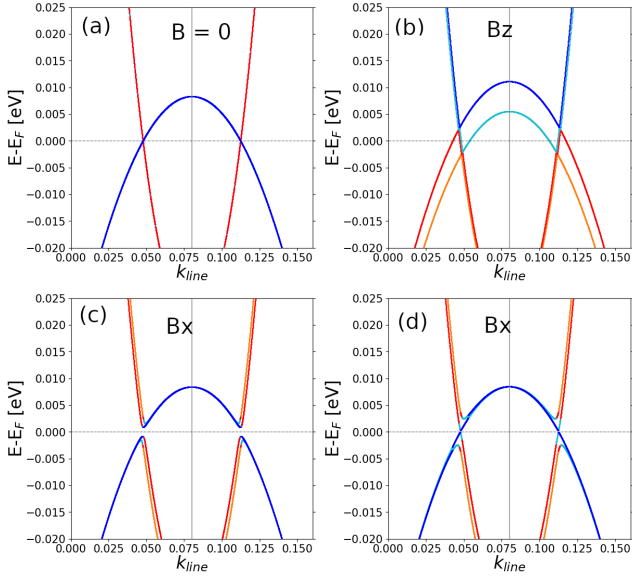


Figure 4. Band structure from Hamiltonian $H_8(\mathbf{k})$. The k -path k_{line} is along the $[001]$ direction and goes from $(0,0,-0.08)$ to $(0,0,+0.08) \text{ \AA}^{-1}$. (a) No applied field. (b) Applied field in the z -direction $\gamma B_z = 2.8 \text{ meV}$. (c) Applied field in the x -direction $\gamma B_x = 2.8 \text{ meV}$, $B_z = B_y = 0$. There is an apparent gap along the k -path at the Dirac points. (d) Applied B_x field and shifted k -path going from $(+\delta k_x, 0, -0.08)$ to $(+\delta k_x, 0, +0.08) \text{ \AA}^{-1}$. The original Dirac points at $(0,0,\pm k_D)$ split into two pair of Weyl points (crossing of 2 bands) at $(\pm\delta k_x, 0, \pm k_D)$ with $\delta k_x = 0.0015 \text{ \AA}^{-1}$.

C. Reconciling the doped and undoped Cd_3As_2 cases

Our electronic structure calculations with the model Hamiltonian have shown that the application of an external magnetic field splits the Dirac point into a pair at Weyl points of opposite chirality. They are displaced symmetrically around kD , possibly with a small energy shift.

Such a behaviour should also, in principle, hold for the band structure of the realistic cases of doped and undoped Cd_3As_2 . In Mn-doped Cd_3As_2 , the gap around $E - E_F = 25 \text{ meV}$ close to Γ is only apparent: the bands do still cross but at a displaced k_x point. Indeed, by plotting the QSGW band structure of Mn-doped Cd_3As_2 along the $Z\Gamma X$ k -path slightly shifted in the k_x direction, one recovers a closed gap as shown in Figure 6. This is where one of the Weyl point has been moved by the field generated by the magnetic impurity.

This implies that the local magnetic field due to the Mn impurity is slightly canted away from the z -direction. This small deviation of the field towards the x -direction is most probably related to spin-orbit coupling in the QSGW Hamiltonian of Mn-doped Cd_3As_2 generating a slight canting away from the z -axis.

Thus, the magnetic impurity does not open a gap in the band structure and one can reasonably well emulate the “exact” band structure of Mn-doped Cd_3As_2 from the band structure of pristine Cd_3As_2 by applying an appropriate external magnetic field. This is clearly seen by comparing Figure 6(b) with Figure 2(c).

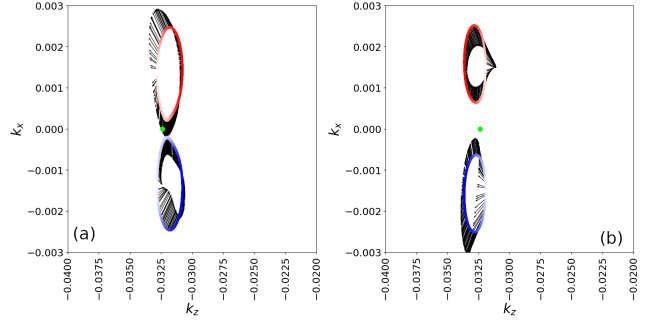


Figure 5. Two-dimensional constant-energy band structure from the $H_8(\mathbf{k})$ Hamiltonian in the $k_z - k_x$ plane around a pair of Weyl points located at $(\pm\delta k_x, 0, -k_D)$. The applied field is $\gamma B_x = 2.8 \text{ meV}$, $B_z = B_y = 0$. The coloring code correspond to the spin component S_z , i.e. blue $S_z = -1$, red $S_z = +1$, white $S_z = 0$. The small arrows represents the spin vector (S_y, S_x) in the $k_z - k_x$ plane. The position of the green dot is $(0, 0, -k_D)$. (a) Constant energy $E = +0.9 \text{ meV}$. (b) Constant energy $E = -0.6 \text{ meV}$. The opposite spin texture (chirality) between the two Weyl points is clear. Also note the change of sign of the spin texture (S_y, S_x) for energy above and below the Weyl crossing points.

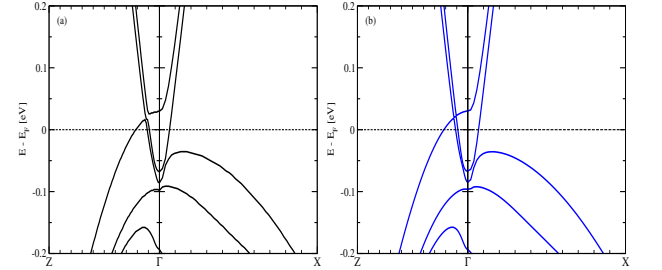


Figure 6. Panel (a): QSGW electronic band structure of Cd_3As_2 for high symmetry k -space path $Z\Gamma X$. Same as panel (d) in Fig. 1. Panel (b): Bands along the $Z\Gamma X$ k -space path slightly shifted in the k_x direction by $\delta k_x = -0.0027 \text{ \AA}^{-1}$ for which the gap is closed. Energies, in eV, are measured from the Fermi level $E_F = 0$. The bands in panel (b) look extremely similar to the bands in panel (c) in Fig. 2.

These results also lead us to believe that one can use the $k \cdot p$ model Hamiltonian, complemented with the Zeeman term for an applied field, to calculate physical properties measured on Mn-doped Cd_3As_2 sample.

D. Conductivity and orientation of the magnetic field

The transport properties of TSMs are intimately related to their band structures. We have seen how the band structure of Cd_3As_2 is modified by magnetic impurity doping and/or by an applied magnetic field. We now turn to studying some effects of a magnetic field on the conductivity of bulk Cd_3As_2 .

In Weyl TSM, an anomalous Hall DC conductivity is observed with a value lying between zero (conductivity of insulators) and one quantum of conductance for topological insulator^{1,33,34}. The DC Hall conductivity, governed by Berry phase, is proportional to the separation in k -space of two Weyl

points which itself may depend on the applied magnetic field.

Magnetotransport of bulk TSM involve additional features not included here (especially the role Landau levels play) and will be discussed elsewhere. In the following we focus on how an applied field affects the symmetry of the dynamical conductivity tensor.

From the eigenstates of $H_g(\mathbf{k})$ and from the velocity matrices $\nabla_{\mathbf{k}} H_g(\mathbf{k})$, we can calculate the conductivity tensor $\sigma_{\alpha\beta}(\omega)$ ($\alpha, \beta = x, y, z$) within linear response theory^{35–40}. Detail of the calculations are provided in Appendix C. In the DC regime, the definition of $\sigma_{\alpha\beta}$ from the Berry curvature⁴⁰ implies that conductivity tensor is anti-symmetric, i.e. $\sigma_{\alpha\beta} = -\sigma_{\beta\alpha}$ for $\alpha \neq \beta$. This is due to the property of the cross product of the current operator matrix elements entering the definition of the Berry curvature⁴⁰.

In the AC regime ($\omega \neq 0$), the anti-symmetry of the conductivity tensor is not obvious, as shown in Appendix C. The symmetry of the conductivity tensor will depend on the intrinsic symmetry of the eigenstates, and therefore on the orientation of the magnetic field. In the following, we show the symmetry of the off-diagonal components $\sigma_{\alpha\beta}(\omega)$ ($\alpha \neq \beta$) for arbitrary orientation of the external magnetic field.

As a first step, we have checked that our calculations satisfy the Onsager relationships, as expected, i.e. $\sigma_{xy}(\omega; B_z) = \sigma_{yx}(\omega; -B_z)$ (and likewise for the xz, zx components with an applied B_y field, and for the yz, zy components with an applied B_x). Different symmetry relationships may hold for arbitrary orientations of the applied field.

The results of our calculations with different field orientations are summarised in Figure 7. For an applied field along the high symmetry Cartesian directions x, y, z , only the (Hall) conductivity in the plane perpendicular to the field is non-zero, as should be expected. For example, with $\mathbf{B} = (0, 0, B_z)$, only the components $\sigma_{xy, yx}$ are non-zero; and similarly for the components xz, zx (yz, zy) components with an applied B_y (B_x). These pairs of components are anti-symmetric, i.e. $\sigma_{\alpha\beta}(\omega) = -\sigma_{\beta\alpha}(\omega)$, similarly to the DC case.

For other orientations of the field, more than one pair of $(\alpha\beta, \beta\alpha)$ components have non-zero conductivity values. This comes essentially from the symmetry of the rotation of the frame-axis and the fact that only the “perpendicular to the field” (non-diagonal) components of the conductivity are non-zero. For field orientation along some symmetry lines $[110]$, $[101]$, $[011]$, we find that there is always at least one pair of $\alpha\beta$ components which provide anti-symmetry. This is a very interesting outcome for the optical properties of TSM^{41–43}. Indeed, the anti-symmetry of the (dynamical) conductivity tensor is a central key in order to obtain non-reciprocity effects of light⁴³ and thermal radiation⁴⁴ in Weyl TSMs.

Our results imply that the local field, whatever its origin, does not need to be strictly oriented along high symmetry Cartesian axis to realize antisymmetry of the optical conductivity tensor, and therefore in order to obtain non-reciprocal effects in Weyl TSMs.

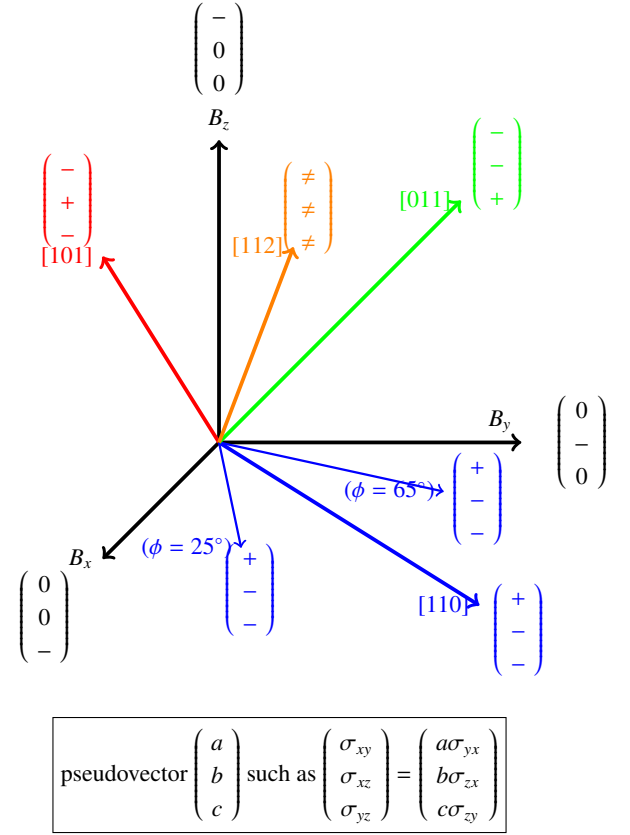


Figure 7. Symmetry of the off-diagonal components of the AC conductivity tensor $\sigma_{\alpha\beta}(\omega)$. For a given field orientation, the symmetry relationships hold for all energy $\omega \neq 0$. The different arrows represent the direction $[hkl]$ of the applied magnetic field in the 3D real space. The pseudovector gives the relationship between the 3 pairs (xy, yx) , (xz, zx) and (yz, zy) of the conductivity components.

III. CONCLUSION

We have studied electronic structure of bulk Cd_3As_2 by using QSGW electronic structure calculations and a $k \cdot p$ model Hamiltonian. We have shown that substitutional doping by Mn impurities, in the small doping regime, induce a topological phase transition, i.e. the original Dirac points in pristine Cd_3As_2 split into individual Weyl points. We have demonstrated that the electronic structure of Mn-doped Cd_3As_2 can be fairly well reproduced by the electronic structure of pristine Cd_3As_2 with an appropriate external magnetic field. This result highlights opportunities for unique device functionality based on band structure tuning which is not found in conventional magnetic Weyl TSM. Using a $k \cdot p$ model Hamiltonian, in the presence of an applied magnetic field, we have studied the conductivity of bulk Cd_3As_2 for different orientations of the applied field and shown the symmetry properties of the conductivity tensor.

From an experimental standpoint, substitutional doping with Mn must first be demonstrated in Cd_3As_2 ¹³, followed by verification of changes in the bandstructure and properties.

At dilute doping, spins will be disordered; causing the net field to be small. However an applied field may act to align the Mn spins, greatly enhancing the spin susceptibility relative to pristine Cd_3As_2 . At higher doping the Mn can interact, and affect the spin ordering and modify the effective field. Also we considered substitutional doping only. The interstitial Mn(I) may act differently from the substitutional Mn(s), especially as Mn(I) will dope the system. Also Mn(I)-Mn(s) interactions can be very different from Mn(s)-Mn(s) interaction, which can affect the thermodynamic distribution of dopants and the total spin.

ACKNOWLEDGMENTS

This work was authored in part by the National Renewable Energy Laboratory for the U.S. Department of Energy (DOE) under Contract No. DE-AC36-08GO28308. Funding was provided by the U.S. Department of Energy (DOE), Office of Science, Basic Energy Sciences, Physical Behavior of Materials Program as part of the “Disorder in Topological Semimetals” project. The views expressed in the article do not necessarily represent the views of the DOE or the U.S. Government. The U.S. Government retains and the publisher, by accepting the article for publication, acknowledges that the U.S. Government retains a nonexclusive, paid-up, irrevocable, worldwide license to publish or reproduce the published form of this work, or allow others to do so, for U.S. Government purposes. We acknowledge the use of the National Energy Research Scientific Computing Center, under Contract No. DE-AC02-05CH11231 using NERSC award BES-ERCAP0021783 and we also acknowledge that a portion of the research was performed using computational resources sponsored by the Department of Energy’s Office of Energy Efficiency and Renewable Energy and located at the National Renewable Energy Laboratory. HN acknowledges financial support from NREL via a subcontract agreement between KCL and NREL.

Appendix A: Questaal calculations

For electronic structure calculations, we use the Quasiparticle Self-Consistent GW approximation^{17–19}. Quasiparticlization of the GW self-energy yields a static one-particle band

$$H_4(\mathbf{k}) = \begin{bmatrix} Ak^2 + E_s & ik_x P_x & ik_y P_y & ik_z P_z + d_{IS} \\ -ik_x P_x & Lk_x^2 + M(k_y^2 + k_z^2) + E_{px} & Nk_x k_y & Nk_x k_z \\ -ik_y P_y & Nk_x k_y & Lk_y^2 + M(k_x^2 + k_z^2) + E_{py} & Nk_y k_z \\ -ik_z P_z + d_{IS} & Nk_x k_z & Nk_y k_z & Lk_z^2 + M(k_x^2 + k_y^2) + E_{pz} \end{bmatrix} \quad (\text{B2})$$

Cubic symmetry is broken by using: $E_{px} = E_{py} = E_p$ and $E_{pz} = E_p - \delta$. The parameter d_{IS} is introduced to break the inversion symmetry²⁰.

The SOC term is

$$H_{SO} = \frac{\Delta}{2} \mathbf{L} \cdot \boldsymbol{\sigma} = \frac{\Delta}{2} \begin{bmatrix} L_z & L_- \\ L_+ & -L_z \end{bmatrix} \quad (\text{B3})$$

similar in form to Hartree–Fock or DFT, but its fidelity is high because the potential is constructed so that energy bands physically correspond to excitation energies. This is because the QSGW self-consistency condition causes the poles of the noninteracting Green’s function to coincide with the interacting one. DFT energy bands, by contrast, have no physical meaning even though they are widely interpreted as excitation energies. See Refs.^{15,16} for further details on the Questaal code and implementation of QSGW.

We use a primitive unit cell, consisting of 80 atoms (48 atoms of Cd and 32 of As), with broken inversion symmetry. The lattice cell vectors are $(-a, a, b)$; $(a, -a, b)$; $(a, a, -b)$ for the pristine Cd_3As_2 system where $a = 6.313747 \text{ \AA}$ and $b = 12.766886 \text{ \AA}$. For the Mn-doped case, one Cd atom is exchanged with one atom of Mn, i.e. corresponding to a doping of $1/48 \sim 2\%$ (an equivalent supercell built from the vectors $(2a, 0, 0)$; $(0, 2a, 0)$; (a, a, b) is used).

For the DFT calculations, a k -point grid of $(4 \times 4 \times 4)$ was used for the DFT calculations. A smaller grid of $(3 \times 3 \times 3)$ was used for QSGW calculations. The self-consistency of the DFT/QSGW calculations is achieved when the RMS change in output-input self-energy and charge density were both converged to about 6×10^{-6} . For QSGW calculations, all the states are used in the present case (5664 states in the total system, with ~ 4612 of them unoccupied). Questaal’s basis set is tailored to the potential¹⁶, so that quasiparticle levels converge much more rapidly with the number of states than what occurs for a plane wave basis. Band structure calculations, in the presence of the GW self-energy, were performed with a denser k -point grid mesh.

Appendix B: The $k \cdot p$ Hamiltonian

The $k \cdot p$ model Hamiltonian^{20,45} is build on 4 bands (s - and p - orbitals) and 2 spins, including spin-orbit coupling (SOC) and a Zeeman-like term:

$$H_8(\mathbf{k}) = H_4(\mathbf{k}) \otimes \mathbb{I}_\sigma + H_{SO} + H_Z. \quad (\text{B1})$$

where \mathbb{I}_σ is the identity in the spin space.

For a given spin, the Hamiltonian $H_4(\mathbf{k})$, in the basis of the s - and p - orbitals, is given by

where $\boldsymbol{\sigma}$ is the vector of Pauli matrices σ_α , L_α are (4×4) matrices in the sp - orbital basis, and $L_\pm = L_x \pm iL_y$ with

For the s - orbital, the angular momentum is zero. Hence we have

$$L_\alpha = \begin{bmatrix} 0 & 0_{3 \times 1} \\ 0_{1 \times 3} & l_\alpha \end{bmatrix} \quad (\text{B4})$$

In the basis of the p - orbitals, the angular momentum is given by

$$l_x = i\hbar \begin{bmatrix} 0 & 0 & 0 \\ 0 & 0 & -1 \\ 0 & 1 & 0 \end{bmatrix}, l_y = i\hbar \begin{bmatrix} 0 & 0 & 1 \\ 0 & 0 & 0 \\ -1 & 0 & 0 \end{bmatrix}, l_z = i\hbar \begin{bmatrix} 0 & -1 & 0 \\ 1 & 0 & 0 \\ 0 & 0 & 0 \end{bmatrix} \quad (\text{B5})$$

The Zeeman term is

$$H_Z = -\gamma \mathbf{B} \cdot \boldsymbol{\sigma} = -\gamma \begin{bmatrix} B_z & B_- \\ B_+ & -B_z \end{bmatrix} \quad (\text{B6})$$

with $B_{\pm} = B_x \pm iB_y$.

In the sp - orbital basis, we take

$$B_{\alpha} = \begin{bmatrix} B_{\alpha}^s & 0 & 0 & 0 \\ 0 & B_{\alpha}^{px} & 0 & 0 \\ 0 & 0 & B_{\alpha}^{py} & 0 \\ 0 & 0 & 0 & B_{\alpha}^{pz} \end{bmatrix} \quad (\text{B7})$$

and apply the B field “uniformly” on the p - orbitals only, i.e. $B_{\alpha}^{px} = B_{\alpha}^{py} = B_{\alpha}^{pz} = B_{\alpha}$ and $B_{\alpha}^s = 0$.

Note that calculations with $B_{\alpha}^s = B_{\alpha}$ do not change significantly the electronic structure around the Dirac point; and not affect the results of the symmetry of the conductivity tensor upon the direction of the applied field.

The value of the parameters are taken from Ref. [20] with a small modification of the SO coupling constant (here we take $\Delta = 0.155$ eV) to make the Dirac points align with the Fermi level E_F within a range of 10^{-5} eV.

Appendix C: Linear response conductivity

The (dynamical) electrical conductivity is obtained from linear response theory and given by^{35,37,38}

$$\sigma_{\alpha\beta}(\omega) = \sigma_{\alpha\beta}^g(\omega) + \frac{e^2}{i\omega} S_{\alpha\beta}(\omega) \quad (\text{C1})$$

where $\sigma_{\alpha\beta}^g(\omega)$ is the so-called gauge term proportional to $\delta_{\alpha\beta}$ ^{35,37,38} and $\alpha, \beta = x, y, z$ the Cartesian coordinates. The current-current correlation function $S_{\alpha\beta}(\omega)$ is

$$S_{\alpha\beta}(\omega) = -2 \int \frac{d\epsilon}{2\pi} f_{\epsilon} \text{Tr} \left[j_{\alpha} \text{Im} G(\epsilon) j_{\beta} G_{+}(\epsilon + \hbar\omega) + j_{\alpha} G_{-}(\epsilon - \hbar\omega) j_{\beta} \text{Im} G(\epsilon) \right] \quad (\text{C2})$$

where f_{ϵ} is the Fermi-Dirac distribution function, $j_{\alpha, \beta}$ the current operators, and G_{\pm} are the Green's functions $G_{\pm} = (\epsilon - H_8(\mathbf{k}) \pm i\eta)^{-1}$ (with $\eta \rightarrow 0^+$) and $\text{Im} G(\epsilon) = \frac{1}{2i}(G_{+} - G_{-}) = -\pi\delta(\epsilon - H_8)$.

Using a compact notation for the eigenstates of $H_8(\mathbf{k})$, $E_n \equiv E_n(\mathbf{k})$ and $|n\rangle \equiv |u_n(\mathbf{k})\rangle$, one recovers the usual expression for the dynamical conductivity $\sigma_{\alpha\beta}(\omega)$ (with $\alpha \neq \beta$)³⁵⁻⁴⁰

$$\begin{aligned} \sigma_{\alpha\beta}(\omega) &= -ie^2\hbar \sum_{n,m \neq n} \left(\frac{f_{E_m} - f_{E_n}}{\hbar\omega} \right) \frac{\langle n|j_{\alpha}|m\rangle \langle m|j_{\beta}|n\rangle}{(E_m - E_n) + \hbar\omega + i\eta} \\ &= \frac{e^2}{i\omega} \sum_{n,m \neq n} (f_{E_n} - f_{E_m}) \frac{\langle n|j_{\alpha}|m\rangle \langle m|j_{\beta}|n\rangle}{(E_n - E_m) - \hbar\omega - i\eta} \end{aligned} \quad (\text{C3})$$

The matrix elements $\langle n|j_{\alpha}|m\rangle$ of the α -component of the current operator are obtained, in the k -space, from the matrix elements $\langle u_n(k)|\nabla_{k_{\alpha}} H_8(\mathbf{k})|u_m(k)\rangle$. Analytical expressions for $\nabla_{k_{\alpha}} H_8(\mathbf{k})$ are readily obtained from Eq.(B2).

Also, note that by swapping the α, β indices, one obtains an expression for $\sigma_{\beta\alpha}(\omega)$ which is clearly different from Eq. C3:

$$\begin{aligned} \sigma_{\beta\alpha}(\omega) &= \frac{e^2}{i\omega} \sum_{n,m \neq n} (f_{E_m} - f_{E_n}) \frac{\langle n|j_{\alpha}|m\rangle \langle m|j_{\beta}|n\rangle}{(E_m - E_n) - \hbar\omega - i\eta} \\ &\neq \sigma_{\alpha\beta}(\omega) \\ &\text{and } \neq -\sigma_{\alpha\beta}(\omega) \end{aligned} \quad (\text{C4})$$

Therefore, unless there is a very specific symmetry in the Hamiltonian, reflected in the spectrum E_n and the eigenstates $|n\rangle$, one cannot easily conclude if the conductivity tensor is symmetric, or anti-symmetric. Also note that, $H_8(\mathbf{k})$ and $\nabla_{k_{\alpha}} H_8(\mathbf{k})$ being Hermitian, is not enough to explain the (anti)symmetry.

Finally, when performing actual calculations, the sums implicitly include the k -dependence of the eigenstates, i.e.

$$\sum_{n,m \neq n} \dots \rightarrow \int \frac{dk}{(2\pi)^3} \sum_{n=1, m \neq n}^8 \dots \quad (\text{C5})$$

Numerical calculations were performed for a regular cubic k -point grid, centered on the Γ point, ranging from -0.08 to 0.08 \AA^{-1} in the three Cartesian directions. A mesh of $(355 \times 355 \times 355)$ was used, i.e. more than 44 millions k -points in order to fully capture the contributions of the Weyl points⁴⁰.

Appendix D: Identification of the Weyl points

In this appendix, we show in detail the spin texture of the bands around the Dirac point at $(0, 0, k_D)$ in Figure 3. We calculate the spin components $S_{x,y,z}$ from expectation value of the Pauli matrices $S_i = \langle \sigma_i \rangle$ using the eigenstates of $H_8(\mathbf{k})$ at each \mathbf{k} point.

In Figure 8, the 2D maps represent the spin vectors (S_y, S_x) in the $k_z - k_x$ plane as black arrows. The color coding of the 2D constant energy contours corresponds to the S_z spin component: blue for minority spin $S_z = -1$, red for majority spin $S_z = 1$, and white for $S_z \sim 0$.

Due to the field applied in the z -direction, the Dirac point is split into individual Weyl points³² located at $(0, 0, k_z = k_D \mp \delta k_W^{\pm})$. The constant energy slices in the Weyl “cones” have elliptic shapes because of the anisotropy of the band velocity in k -space. The Weyl points are shifted in energy from E_F by the Zeeman effect, down by $-E_W^+$ for the Weyl point W^+ with majority spin along the z -direction, and shifted up by

$+E_W^-$ for the Weyl point W^- with minority S_z spin directed in the opposite direction of the applied field (see red and blue ellipses in Fig. 8 respectively).

Let us first focus on the Weyl point W^- above E_F . For energies above the Weyl point (i.e. $E - E_F > +E_W^-$), the spin vectors (S_y, S_x) are directed outwards the blue ellipses, while for energies below the Weyl point the spin vectors (S_y, S_x) are directed inwards.

The other Weyl point W^+ , located below E_F , has the opposite chirality as expected. That is for energies $E - E_F > -E_W^+$ above the Weyl point, the spin vectors (S_y, S_x) are directed inwards the red ellipses, while for energies below the Weyl point the spin vectors (S_y, S_x) are directed outwards.

Note that the constant energy slices of a given Weyl “cone”, i.e. blue or red ellipses for W^\pm (with Chern number ± 1 according to Ref³²), are accompanied with another band (red or blue respectively) with opposite spin S_z direction which originates from the other Weyl “cone” W^\pm (at opposite energy).

The two other crossings, labelled C^\pm in Figure 9(a), have been identified as other Weyl points associated with higher Chern number in Ref³². Our results reflect a different picture for the C^\pm points, and the difference can be important because of the central role spin texture plays in transport properties of TSM. For example, the (anomalous) Hall conductivity is given in terms of the Berry curvature^{32,40}.

From the eigenstates of $H_8(\mathbf{k})$, we can calculate the ($\gamma = x, y, z$) components of the Berry curvature $\Omega_{n,\gamma}$ for a given eigenstate n as follows:

$$\Omega_{n,\gamma} = i\hbar^2 \sum_{m \neq n} \frac{\langle n|j_\alpha|m\rangle\langle m|j_\beta|n\rangle - \langle n|j_\beta|m\rangle\langle m|j_\alpha|n\rangle}{(E_n - E_m)^2} \quad (\text{D1})$$

with $\gamma \neq \alpha, \beta$ and $\alpha \neq \beta$.

Figure 9 shows two 3D maps, in the k -space, of the Berry curvature vectors ($\bar{\Omega}_x, \bar{\Omega}_y, \bar{\Omega}_z$) as blue arrows. We have intentionally displayed the arrows as short arrows in order to avoid strong overlap of the different vectors at different k -points which may lead to confusion. The quantities $\bar{\Omega}_\gamma$ come from the summation of $\Omega_{n,\gamma}$ over an chosen energy window $E_n \in [E_{\min}, E_{\max}]$. We have choosen energy windows around the pairs $(W, C)^\pm$ to check which of the crossing points provide the more Berry curvature. In Fig. 9(b), the summation is performed for the energy window $[+3, +12.5]$ meV around the pair of W^- and C^- crossing points; in Fig. 9(c) for the energy window $[-12.5, -3]$ meV around the pair of W^+ and C^+ crossings. The line of symbols, at $k_x = k_y = 0$, represent the sequence of C^+, W^+, D, W^-, C^- points along k_z , with the Dirac point D at $(0, 0, k_D)$. For both integration windows, one can clearly see a large contribution of Berry curvature around the Weyl points W^\pm (black dots) in comparison to a smaller Berry curvature around the crossing points C^\pm (green diamonds). This tends to indicate that, amongst the four band crossings $(W, C)^\pm$, the Weyl points W^\pm will be playing a more important role in the transport properties based on Berry curvatures.

We have not attempted to analyze why Ref³² and this work arrive at different conclusions about the C^\pm points. The discrepancy can probably be traced to a difference in the construction of the k.p hamiltonians.

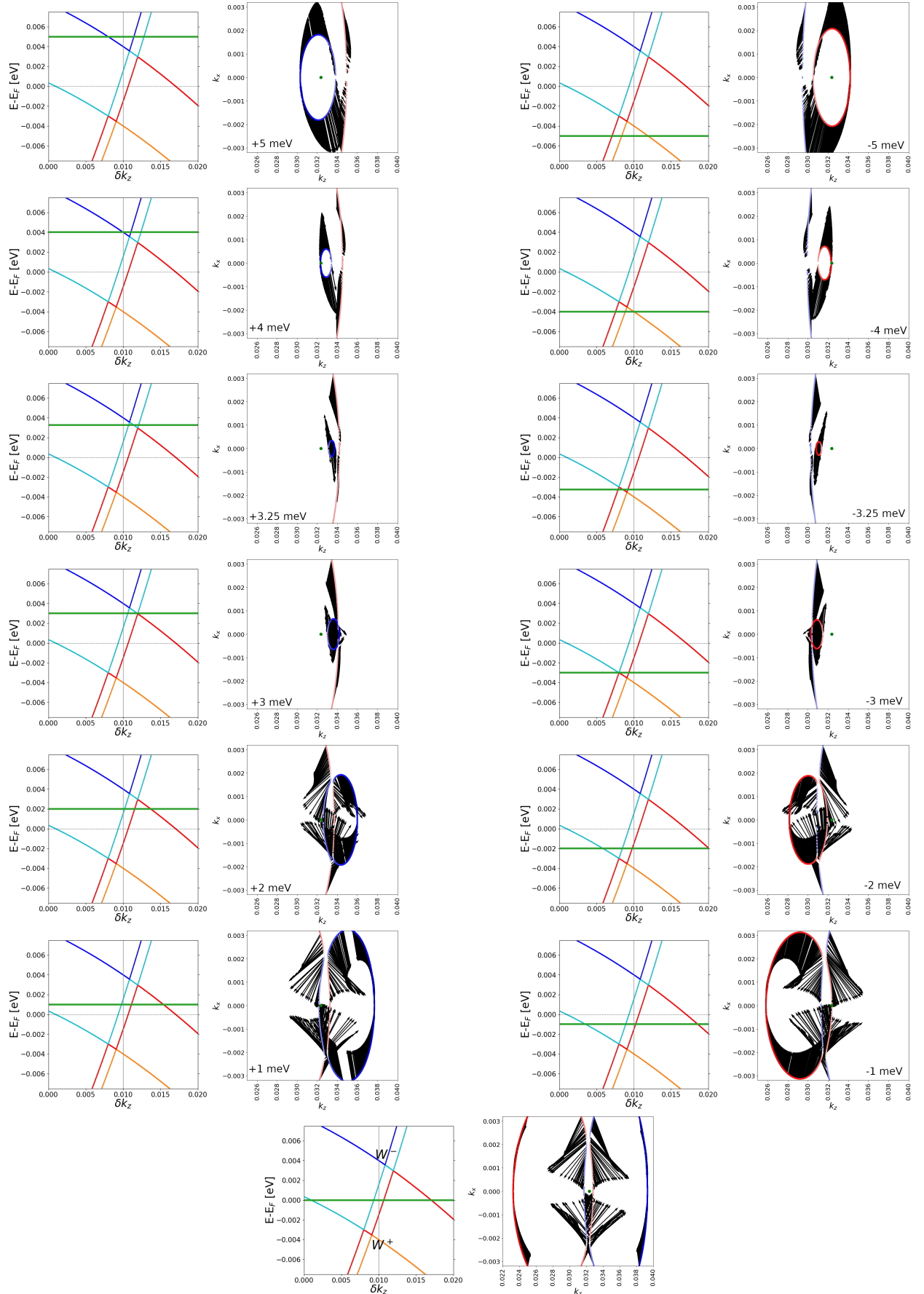


Figure 8. Left and Right double-column panels show the band structure (left side in a double-column) along k_z path and the 2D maps of constant-energy band structure (right side in a double-column) in the $k_z - k_x$ plane around the Dirac point (green dot). The constant energy is shown by the horizontal green solid-line in the k_z bands. The applied field is $\gamma B_z = 4$ meV. The band coloring in the 2D maps corresponds to the value of S_z , i.e. blue $S_z = -1$, red $S_z = +1$, white $S_z = 0$. The black arrows correspond the spin vectors (S_y, S_x) in the $k_z - k_x$ plane.

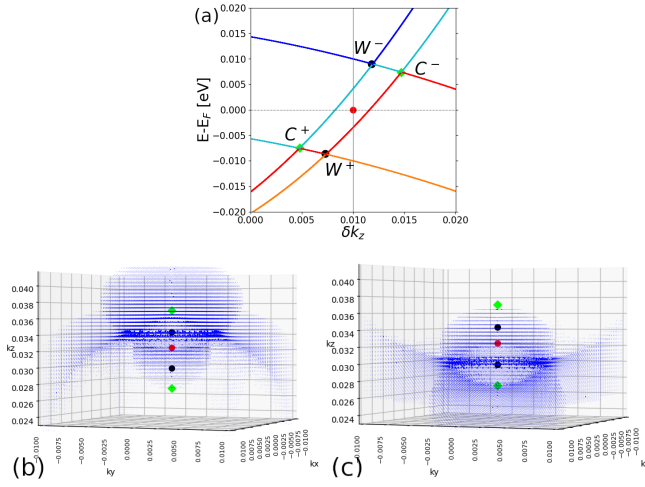


Figure 9. Panel (a): Band structure with the Weyl points, W^+ and W^- (black dots) and crossings C^+ and C^- (green diamonds) for an applied field is $\gamma B_z = 10$ meV. The red dot represents the original Dirac point. Panel (b,c): 3D maps, on regular k -space grid, of the Berry curvature vectors ($\bar{\Omega}_x, \bar{\Omega}_y, \bar{\Omega}_z$) (small blue arrows). The line of symbols, at $k_x = k_y = 0$, represent the sequence of C^+, W^+, D, W^-, C^- points along k_z , with the Dirac point D (red dot) at $k_z = k_D = 0.032 \text{ \AA}^{-1}$. A larger contribution of Berry curvature is found around the Weyl points W^\pm (black dots) than around the C^\pm crossing points (green diamonds). Energy window integration for $\bar{\Omega}_y$ is around the pair of points W^-, C^- (located above the D point, $k_z > k_D$) in panel (b); around the pair C^+, W^+ (located below the D point, $k_z < k_D$) in panel (c).

- ¹ N. P. Armitage, E. J. Mele, and A. Vishwanath, Weyl and Dirac semimetals in three-dimensional solids, *Rev. Mod. Phys.* **90**, 015001 (2018).
- ² J. Li, Z. Zhang, C. Wang, H. Huang, B.-L. Gu, and W. Duan, Topological semimetals from the perspective of first-principles calculations, *Journal of Applied Physics* **128**, 191101 (2020).
- ³ T. Liang, Q. Gibson, M. N. Ali, M. Liu, R. J. Cava, and N. P. Ong, Ultrahigh mobility and giant magnetoresistance in the Dirac semimetal Cd_3As_2 , *Nature Materials* **14**, 280 (2015).
- ⁴ A.-Q. Wang, X.-G. Ye, D.-P. Yu, and Z.-M. Liao, Topological Semimetal Nanostructures: From Properties to Topotronics, *ACS Nano* **14**, 3755 (2020).
- ⁵ Q. L. He, T. L. Hughes, N. P. Armitage, Y. Tokura, and K. L. Wang, Topological spintronics and magnetoelectronics, *Nature Materials* **21**, 15 (2022).
- ⁶ B. A. Bernevig, C. Felser, and H. Beidenkopf, Progress and prospects in magnetic topological materials, *Nature* **603**, 41 (2022).
- ⁷ W. J. Lee, Y. A. Salawu, H.-J. Kim, C. W. Jang, S. Kim, T. Ratcliff, R. G. Elliman, Z. Yue, X. Wang, S.-E. Lee, M.-H. Jung, J.-S. Rhyee, and S.-H. Choi, Possible permanent Dirac- to Weyl-semimetal phase transition by ion implantation, *NPG Asia Materials* **14**, 31 (2022).
- ⁸ L.-L. Wang, N. H. Jo, B. Kuthanazhi, Y. Wu, R. J. McQueeney, A. Kaminski, and P. C. Canfield, Single pair of Weyl fermions in the half-metallic semimetal EuCd_2As_2 , *Phys. Rev. B* **99**, 245147 (2019).
- ⁹ J.-Z. Ma, S. M. Nie, C. J. Yi, J. Jandke, T. Shang, M. Y. Yao, M. Naamneh, L. Q. Yan, Y. Sun, A. Chikina, V. N. Strocov, M. Medarde, M. Song, Y.-M. Xiong, G. Xu, W. Wulfhekel, J. Mesot, M. Reticcioli, C. Franchini, C. Mudry, M. Müller, Y. G. Shi, T. Qian, H. Ding, and M. Shi, Spin fluctuation induced Weyl semimetal state in the paramagnetic phase of EuCd_2As_2 , *Science Advances* **5**, 4718 (2019).
- ¹⁰ D. Santos-Cottin, I. Mohelský, J. Wyzula, F. Le Mardelé, I. Kapon, S. Nasrallah, N. Barišić, I. Živković, J. R. Soh, F. Guo, K. Rigaux, M. Puppín, J. H. Dil, B. Gudac, Z. Rukelj, M. Novak, A. B. Kuzmenko, C. C. Homes, T. Dietl, M. Orlita, and A. Akrap, EuCd_2As_2 : A Magnetic Semiconductor, *Phys. Rev. Lett.* **131**, 186704 (2023).
- ¹¹ Y. Shi, Z. Liu, L. A. Burnett, S. Lee, C. Hu, Q. Jiang, J. Cai, X. Xu, M. Li, C.-C. Chen, and J.-H. Chu, Absence of weyl nodes in EuCd_2As_2 revealed by the carrier density dependence of the anomalous Hall effect, *Phys. Rev. B* **109**, 125202 (2024).
- ¹² S. Nishihaya, A. Nakamura, M. Ohno, M. Kriener, Y. Watanabe, M. Kawasaki, and M. Uchida, Intrinsic insulating transport characteristics in low-carrier density EuCd_2As_2 films, *Applied Physics Letters* **124**, 023103 (2024).
- ¹³ A. D. Rice, I. A. Leahy, H. Ness, M. van Schilfgaarde, and K. Alberi, unknown, (unpublished) (2025).

- ¹⁴ Z. K. Liu, J. Jiang, B. Zhou, Z. J. Wang, Y. Zhang, H. M. Weng, D. Prabhakaran, S.-K. Mo, H. Peng, P. Dudin, T. Kim, M. Hoesch, Z. Fang, X. Dai, Z. X. Shen, D. L. Feng, Z. Hussain, and Y. L. Chen, A stable three-dimensional topological Dirac semimetal Cd_3As_2 , *Nature Materials* **13**, 677 (2014).
- ¹⁵ Questaal code website, <https://www.questaal.org>.
- ¹⁶ D. Pashov, S. Acharya, W. R. Lambrecht, J. Jackson, K. D. Belashchenko, A. Chantis, F. Jamet, and M. van Schilfgaarde, Questaal: A package of electronic structure methods based on the linear muffin-tin orbital technique, *Comput. Phys. Commun.* **249**, 107065 (2020).
- ¹⁷ S. V. Faleev, M. van Schilfgaarde, and T. Kotani, All-electron self-consistent *GW* approximation: Application to Si, MnO, and NiO, *Phys. Rev. Lett.* **93**, 126406 (2004).
- ¹⁸ M. van Schilfgaarde, T. Kotani, and S. Faleev, Quasiparticle Self-Consistent *GW* Theory, *Phys. Rev. Lett.* **96**, 226402 (2006).
- ¹⁹ T. Kotani, M. van Schilfgaarde, and S. V. Faleev, Quasiparticle self-consistent *GW* method: A basis for the independent-particle approximation, *Phys. Rev. B* **76**, 165106 (2007).
- ²⁰ Z. Wang, H. Weng, Q. Wu, X. Dai, and Z. Fang, Three-dimensional Dirac semimetal and quantum transport in Cd_3As_2 , *Phys. Rev. B* **88**, 125427 (2013).
- ²¹ M. N. Ali, Q. Gibson, S. Jeon, B. B. Zhou, A. Yazdani, and R. J. Cava, The crystal and electronic structures of Cd_3As_2 , the three-dimensional electronic analogue of graphene, *Inorganic Chemistry* **53**, 4062 (2014).
- ²² A. Mosca Conte, O. Pulci, and F. Bechstedt, Electronic and optical properties of topological semimetal Cd_3As_2 , *Scientific Reports* **7**, 45500 (2017).
- ²³ I. Crassee, R. Sankar, W.-L. Lee, A. Akrap, and M. Orlita, 3D Dirac semimetal Cd_3As_2 : A review of material properties, *Phys. Rev. Mater.* **2**, 120302 (2018).
- ²⁴ S. Yue, H. T. Chorsi, M. Goyal, T. Schumann, R. Yang, T. Xu, B. Deng, S. Stemmer, J. A. Schuller, and B. Liao, Soft phonons and ultralow lattice thermal conductivity in the Dirac semimetal Cd_3As_2 , *Phys. Rev. Res.* **1**, 033101 (2019).
- ²⁵ E. Kulatov, Y. Uspenskii, L. Oveshnikov, A. Mekhiya, A. Davydov, A. Ril', S. Marenkin, and B. Aronzon, Electronic, magnetic and magnetotransport properties of Mn-doped Dirac semimetal Cd_3As_2 , *Acta Materialia* **219**, 117249 (2021).
- ²⁶ C. Brooks, M. van Schilfgaarde, D. Pashov, J. N. Nelson, K. Alberi, D. S. Dessau, and S. Lany, Band energy dependence of defect formation in the topological semimetal Cd_3As_2 , *Phys. Rev. B* **107**, 224110 (2023).
- ²⁷ S. Jeon, B. B. Zhou, A. Gyenis, B. E. Feldman, I. Kimchi, A. C. Potter, Q. D. Gibson, R. J. Cava, A. Vishwanath, and A. Yazdani, Landau quantization and quasiparticle interference in the three-dimensional Dirac semimetal Cd_3As_2 , *Nature Materials* **13**, 851 (2014).
- ²⁸ J. N. Nelson, I. A. Leahy, A. D. Rice, C. Brooks, G. Teeter, M. van Schilfgaarde, S. Lany, B. Fluegel, M. Lee, and K. Alberi, Direct link between disorder and magnetoresistance in topological semimetals, *Phys. Rev. B* **107**, L220206 (2023).
- ²⁹ E. G. Maksimov, I. I. Maxin, S. Y. Savrasov, and Y. A. Uspenski, Excitation spectra of semiconductors and insulators: a density-functional approach to many-body theory, *Journal of Physics: Condensed Matter* **1**, 2493 (1989).
- ³⁰ M. van Schilfgaarde and M. I. Katsnelson, First-principles theory of nonlocal screening in graphene, *Phys. Rev. B* **83**, 081409 (2011).
- ³¹ M. Grüning, A. Marini, and A. Rubio, Density functionals from many-body perturbation theory: The band gap for semiconductors and insulators, *J. Chem. Phys.* **124**, 154108 (2006).
- ³² S. Baidya and D. Vanderbilt, First-principles theory of the Dirac semimetal Cd_3As_2 under Zeeman magnetic field, *Phys. Rev. B* **102**, 165115 (2020).
- ³³ A. A. Burkov and L. Balents, Weyl semimetal in a topological insulator multilayer, *Phys. Rev. Lett.* **107**, 127205 (2011).
- ³⁴ I. Panfilov, A. A. Burkov, and D. A. Pesin, Density response in Weyl metals, *Phys. Rev. B* **89**, 245103 (2014).
- ³⁵ A. Bastin, C. Lewiner, O. Betbeder-Matibet, and P. Nozieres, Quantum oscillations of the Hall effect of a Fermion gaz with random impurity scattering, *J. Phys. Chem. Solids* **32**, 1811 (1971).
- ³⁶ A. Crépieux and P. Bruno, Theory of the anomalous Hall effect from the Kubo formula and the Dirac equation, *Phys. Rev. B* **64**, 014416 (2001).
- ³⁷ H. Bruus and K. Flensberg, *Many-Body Quantum Theory in Condensed Matter Physics: An Introduction* (Oxford University Press, Oxford, 2004).
- ³⁸ F. T. Vasko and O. E. Raichev, *Quantum Kinetic Theory and Applications: Electrons, Photons, Phonons* (Springer, New York, 2005).
- ³⁹ T. Morimoto and H. Aoki, Flow diagram of the longitudinal and Hall conductivities in ac regime in the disordered graphene quantum hall system, *Journal of Physics: Conference Series* **400**, 042047 (2012).
- ⁴⁰ M. Gradhand, D. V. Fedorov, F. Pientka, P. Zahn, I. Mertig, and B. L. Györfy, First-principle calculations of the Berry curvature of Bloch states for charge and spin transport of electrons, *Journal of Physics: Condensed Matter* **24**, 213202 (2012).
- ⁴¹ O. V. Kotov and Y. E. Lozovik, Dielectric response and novel electromagnetic modes in three-dimensional Dirac semimetal films, *Phys. Rev. B* **93**, 235417 (2016).
- ⁴² J. Hofmann and S. Das Sarma, Surface plasmon polaritons in topological Weyl semimetals, *Phys. Rev. B* **93**, 241402 (2016).
- ⁴³ O. V. Kotov and Y. E. Lozovik, Giant tunable nonreciprocity of light in Weyl semimetals, *Phys. Rev. B* **98**, 195446 (2018).
- ⁴⁴ B. Zhao, C. Guo, C. A. C. Garcia, P. Narang, and S. Fan, Axion-field-enabled nonreciprocal thermal radiation in Weyl semimetals, *Nano Letters* **20**, 1923 (2020).
- ⁴⁵ M. Smith, V. L. Quito, A. A. Burkov, P. P. Orth, and I. Martin, Theory for Cd_3As_2 thin films in the presence of magnetic fields, *Phys. Rev. B* **109**, 155136 (2024).